Water Formation and Destruction by Powerful X-ray Flares from a T-Tauri Star

An Honors Thesis (HONR 499)

by

Abygail R. Waggoner

Thesis Advisors

Dr. L. Ilsedore Cleeves and Dr. Patricia Lang

Ball State University
Muncie, Indiana

April 2018

Expected Date of Graduation

May 2018

Abstract

Young stars emit strong flares of X-ray radiation that penetrate the surface layers of their associated protoplanetary disks. It is still an open question as to whether flares create significant disk chemical composition changes. We present models of the time-evolving chemistry of *gaseous* H_2O during X-ray flaring events. The chemistry is modeled at point locations in the disk between 1 and 20 AU at various vertical heights from the mid-plane to the surface. We find the gas-phase H_2O abundance can be enhanced in the surface (Z/R $\geq$ 0.3) by more than a factor of $\sim 3-5$ by strong flares, i.e., those that increase the ionization rate by a factor of 100. Dissociative recombination of H_3O^+, H_2O adsorption onto grain, and photolysis of H_2O are found to be the three dominant processes leading to a change in H_2O abundance. We find X-ray flares have predominantly short-term (days) effects on *gaseous* H_2O abundance, but some regions show a long-term (for the duration of the test $\sim$ 15 days) decrease in *gaseous* H_2O due to adsorption onto grains as ice, though only in regions with otherwise low water ice abundances. Even though we do not see a substantial increase in long term water (gas+ice) production, the flares large effects should be detectable as time varying inner disk water "bursts" with future observations from facilities like JWST.

Acknowledgments

This research began during Summer 2017, where it was funded by the Smithsonian Astronomical Observatory Research Experience for Undergraduates (SAO REU) program. SAO REU was funded by the National Science Foundation REU and Department of Defense ASSURE programs under NSF Grant AST-1659473, and by the Smithsonian Institution.

Thanks to Ilse Cleeves, my advisory and mentor on this research project though Summer 2017 and the 2017-2018 academic year.

Thanks also go to Dr. James Poole for mentoring my undergraduate research studies on hydroxyl radical research and computation chemistry studies.

Thanks to the National Science Foundation Graduate Research Foundation Program, who awarded me a 3 year graduate school fellowship to continue this research in my graduate studies starting in Fall 2018.

Contents

Abstract ii

Acknowledgments iii

1 Process Analysis Statement 1

2 Introduction 3

3 Model and Methods 6
- 3.1 Model . . . 6
- 3.2 Methods . . . 7

4 Results 10
- 4.1 Physical Trends in the Disk . . . 10
- 4.2 Analysis of Different H_2O Response Curves . . . 12
  - 4.2.1 Type 1: Net Destruction . . . 12
  - 4.2.2 Type 2: Net Production with Fast Decay (< 14 days) . . . 14
  - 4.2.3 Type 3: Net Production with Long Term Increase (> 14 days) . . . 15
  - 4.2.4 Type 4: Hybrid . . . 16
  - 4.2.5 Type 5: No Response . . . 17
- 4.3 Response Trends in the Disk . . . 18
- 4.4 Ice H_2O Responses . . . 19
- 4.5 Impacts of Muli-flare Events . . . 21
- 4.6 Flare Strength Variation . . . 21

5 Discussion 23
- 5.1 X-ray Ionization Rate and Density Relate to Flare Response Magnitude . . . 23
- 5.2 Relationship Between UV Flux and Temperature to Photolysis or Adsorption Consumption of H_2O . . . 25
- 5.3 Future Goals . . . 25

6 Summary **27**

7 Appendix **30**

CHAPTER 1

Process Analysis Statement

I began research for this thesis in July 2017 during a Research Experience Undergraduate Program at the Harvard Smithsonian Center for Astrophysics under the mentorship of Dr. Ilsedore Cleeves. Dr. Cleeves adapted the chemical model described by Fogel et al. (2011) to simulate X-ray flaring events in protoplanetary disk environments. While the model includes a total of 647 different chemical species, I chose to perform an in-depth analysis on water responses to X-ray flares, instead of a generalized overview of many molecules/atoms.

To begin data collection for this thesis, I used the model to observe H_2O responses at 20 point locations throughout the disk. Each point represents a different physical environment and distance from the central star. I then analyzed each of the 20 points and categorized each curve as one of 5 different types of responses. I then performed a rate analysis at representative points for each of the 5 types of responses to understand which reactions and processes were responsible for changes in H_2O abundance.Rate analysis performed for this thesis was done on responses to a single strong flare. In addition to the single flare, I also modeled events with multiple flares and flares with varying strengths. Lastly, I related physical components of the disk environment, including density, temperature, X-ray ionization rate, and UV flux, to the reactions and processes responsible for changes in H_2O abundance. This will allow us to predict H_2O responses to X-ray flares at point locations within protoplanetary disks based on their physical environment.

The subject of this thesis is only just the beginning of an in depth analysis on chemical responses to stellar radiation in protoplanetary disk environments. This type of research is important to the scientific community, as it will result in more accurate protoplanetary disk models that broaden our understanding of what processes are most relevant in setting the composition of planetesimals, including the composition of our own Solar System bodies. More accurate models will aid astronomers searching for habitable exoplanets, since we will be able to more accurately predict which regions of a planetary system will be most likely to contain life-sustaining molecules based on their location in protoplanetary disks.

In addition, this research will someday help assess whether more active young stars

lead to a more prebiotically rich chemistry, or if high degrees of X-ray variability tend to be more molecularly destructive in protoplanetary disks. Findings will be disseminated to a variety of scientific fields to increase our understanding of possible origins of life. The emergence of biotic molecules is of interest beyond the science community, and is a phenomenon that all of humanity has sought to understand since the beginning of history.

CHAPTER 2

Introduction

Protoplanetary disks are flared dusty accretion disks surrounding young star(s) (Ardila et al., 2002; Bergin et al., 2007; Williams & Cieza, 2011) that form planetary systems (Henning & Semenov, 2013; Stahler & Palla, 2005; Williams & Cieza, 2011). There are four main stages in the formation of a planetary system:

1) Molecular gas clouds collapse due to gravitational forces overcoming support from magnetic, gas, and rotational forces (Stahler & Palla, 2005),
2) Collapse leads to the formation of a new star surrounded by an accretion disk embedded in a molecular envelope,
3) The molecular envelope dissipates, leaving a protoplanetary disk (Henning & Semenov, 2013),
4) Dust grains in the disk collide and stick together to form planetesimals around the star, forming a new planetary system (Williams & Cieza, 2011).

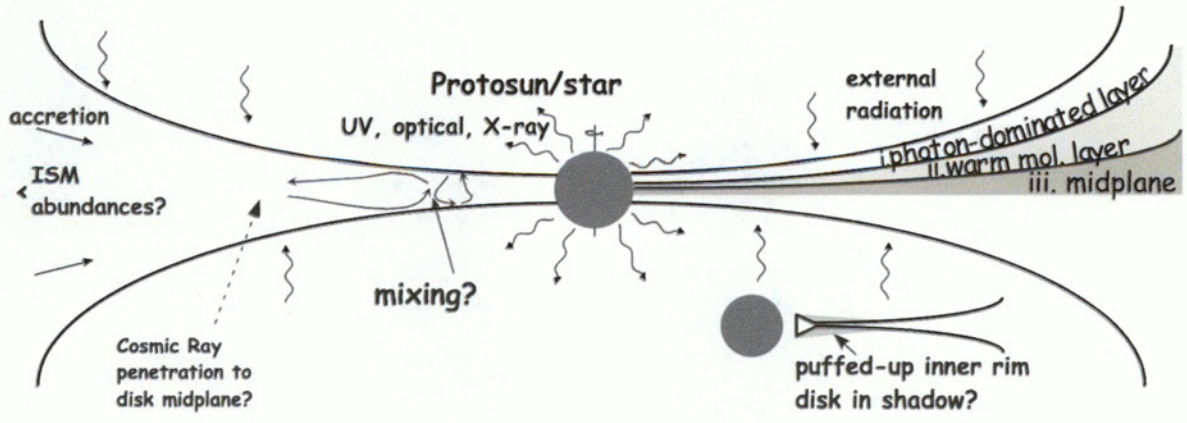

FIGURE 2.1 Image obtained from Bergin et al. (2007). Disks have a flared shape with three layers. (1) The photon dominated layer, (2) the warm molecular layer, and (3) the frozen out mid-planes. Internal radiation from the young star and external radiation are able to penetrate the proton dominated layer, and partially penetrate the warm molecular layer. Temperature is highest in the photon dominated layer, and coolest in the mid-planes. Temperature decreases with increasing radial distance.

These planetary systems are similar to our own Solar System, in the sense that both terrestrial planets and gas giants can form. The composition of these planets is likely affected by the physical and chemical processes that occur during their formation in the protoplanetary disk stage, therefore it is necessary to understand these processes in order to create accurate models of planetary system formation. Observations have shown that protoplanetary disks are flared dusty disks with radii as large as hundreds of AU (Ardila et al., 2002) composed of three layers:

1) The photon-dominated region (PDR), which is rich in photons and atoms.
2) The middle, warm molecular layer, where molecular and radical chemicals can exist.
3) The mid-plane freeze out layer, where molecular and atomic ices can form on dust grains, see Figure 2.1 (Bergin et al., 2007).

Temperatures can range from hundreds of Kelvin to below ten Kelvin. Temperature decreases with increasing disk radius, and temperature decreases with increasing disk depth, largely due to a decrease in internal and external sources of radiation (Williams & Cieza, 2011). Radiation is unable to reach the inner layers of the disk due to the high opacities. For example, the UV flux directly irradiates the PDR, resulting in a temperature increase. Some photons can penetrate the warm molecular layer, but little to no photons reach the mid-plane (Fogel et al., 2011). Photon penetration depth is dependent on the disk density structure. Photons can easily penetrate the PDR since it is a low density area with little protection. However, as the mid-plane is approached density increases, and photons collide with particles in dense regions and scatter. Gas/dust density, temperature, and radiation fields of a typical disk are shown in Figure 2.2

Short-term X-ray flaring is common in solar mass stars (Montmerle & Casanova, 1996), and can produce enough X-rays to penetrate the surrounding disk. All of these discussed factors, especially the presence of high energy photons like X-rays, influence the chemistry of the disk, which evolves over the disk lifetime of $\sim 3-10$ Myr. Most chemicals observed in protoplanetary disks are small and simple molecules that can also exist as radicals and ions, for example CO, HCO^+, CN, HCN, CS, C_2H, and N_2H^+. Some complex molecules, such as formaldehyde, have also been observed (Aikawa et al., 2003; Dutrey et al., 1997, 2007).

Among these chemicals H_2O is one of the most important, owing to its role in the formation of habitable planets like Earth. H_2O ice (referred to as $H_2O_{(gr)}$ in the present thesis) forms on grains in the protoplanetary disk, which enables grains to stick together when they collide. It is believed that both terrestrial and gas giants' rocky inner cores are formed from long-term ($\sim$5Myr) inelastic grain collisions. Without an ice coating, the grains bounce off each other in an elastic collision, which suggests that planet formation is impacted by the presence of $H_2O_{(gr)}$. Since $H_2O_{(gr)}$ is produced from the adsorption of

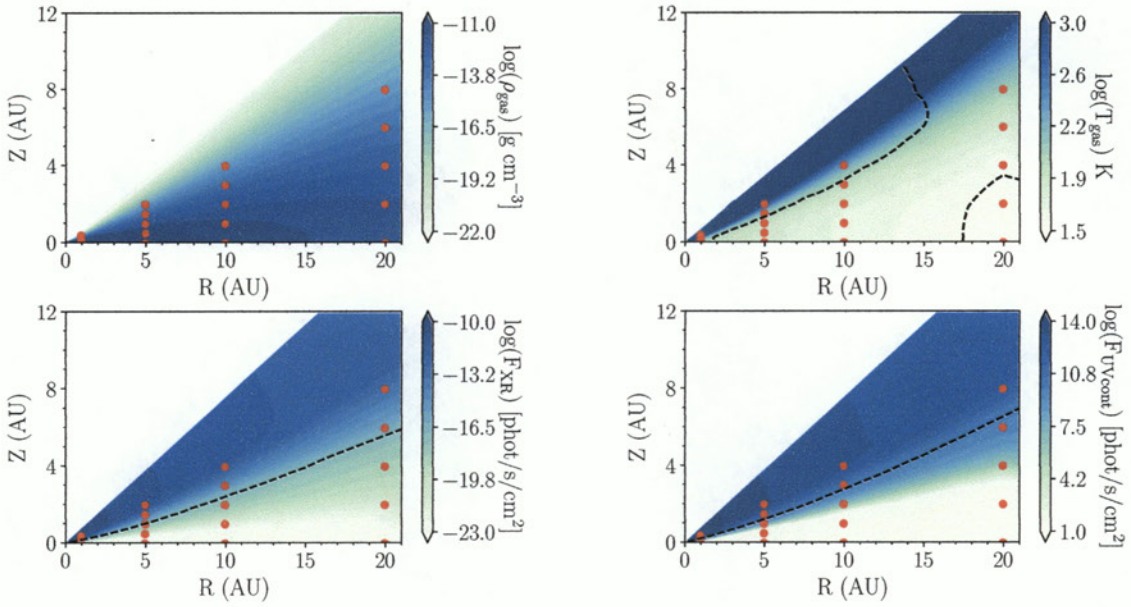

FIGURE 2.2 These plots density, temperature, X-ray ionization rate, and UV flux in the IM Lup protoplanetary disk, a disk encircling a solar-mass young star.Red dots indicate the 20 locations modelled and analyzed in this paper.

gaseous H_2O onto grains, it is essential to understand the how *gaseous* H_2O responds to the physical conditions of the disk.

As discussed above, most of the global chemistry of the disk occurs slowly, however there is some possibility that short-term X-ray activity can impact the composition of the disk. Until recently, X-ray flares were considered negligible when studying chemical activities in protoplanetary disks. However, Cleeves et al. (2017) recently found that the abundance of HCO^+ was time variable in the IM Lup protoplanetary disk. One possible explanation for the observations is chemistry induced by an X-ray flare. This suggests that X-ray radiation and ionization may play an important role in disk chemistry. Like HCO^+, H_2O is sensitive to the ionization state of gas, as most processes that form water involve the initial ionization of H_2 (Cleeves et al., 2014). Thus, it is of interest to understand how water responds to X-ray events. This project examines chemistry impacted by X-ray flares emitted from a T-Tauri star, a star similar to our own in the early ages of its life. This project uses a theoretical model to understand how a dynamic X-ray radiation field effects both instantaneous (~days) and long-term (~Myr) H_2O abundances in a protoplanetary disk, and to identify key species and processes contributing to H_2O vapor changes.

CHAPTER 3

Model and Methods

3.1 Model

To model the chemistry in a dynamic X-ray environment we adopt the model from Fogel et al. (2011), which includes 647 species and 5944 processes known to take place in protoplanetary disks. The code adopts the rate equation method (Wakelam et al., 2013) and calculates the non-equilibrium chemistry as a function of time. Initial chemical conditions were taken from an interstellar cloud model and are shown in Table 3.1 (Cleeves et al., 2016). All chemical abundances are presented with respect to number of hydrogen atoms. The code begins with the initial chemical abundances listed in Table 3.1 , which are designed to be representative of molecular cloud abundances. The code runs for 0.5 Myr to reach a pseudo steady state equilibrium at the time of the flare. The code then slows down to calculate the chemistry during the event with fine resolution (30 minute time steps).

TABLE 3.1 Initial Chemical Abundances

H_2	5×10^{-1}	Mg^+	1×10^{-11}
$H_2O_{(gr)}$	2.5×10^{-4}	Fe^+	1×10^{-11}
O	1×10^{-8}	CO	1.4×10^{-4}
O_2	1×10^{-8}	^{13}CO	2×10^{-6}
He	1.4×10^{-1}	C	5×10^{-9}
N_2	2.25×10^{-5}	NH_3	8×10^{-8}
CN	6×10^{-8}	HCN	2×10^{-8}
H_3^+	1×10^{-8}	C^+	1×10^{-10}
S^+	1×10^{-11}	HCO^+	9×10^{-9}
Si^+	1×10^{-11}	$H^{13}CO^+$	1.286×10^{-10}
C_2H	8×10^{-9}		

Abundances are presented with respect to number of hydrogen atoms, and come from Aikawa et al. (1999)

Gas density (ρ), gas temperature (T_{gas}), dust temperature (T_{dust}), UV Flux, and X-ray ionization rate are changed to simulate different points in the disk. Points are labeled by their radial distance from the star (R) and vertical distance from the mid-plane (Z/R). These factors are taken into account when pre-flare computing pseudo steady state chemistry. The disk is assumed to be azimuthally symmetric and symmet-

ric about the mid-plane. The model ignores any interactions between horizontal zones, although the effect of particle mixing between disk regions is unknown since it cannot be tested with this model (Fogel et al., 2011).

IM Lup is the first observed source to show chemical variability due to an X-ray flare (Cleeves et al., 2017) and is used to define the underlying physical structure of the T-Tauri star and disk model (Cleeves et al., 2016). Parameters for the central star are as follows: effective temperature of $T_{eff} = 3900$ K, stellar radius of 2.5 $R_\odot$ (Pinte et al., 2008), stellar mass of 1 $M_\odot$. (Panić et al., 2009), which is held fixed as was done in Cleeves et al. (2016).

The Smith et al. (2004) Ohio State University (OSU) gas-phase chemical network was used as a basis for the chemical network, and Hasegawa et al. (1992) was used to model grain-surface chemistry. The five types of chemical and physical processes used in the model include:

1) dissociative recombination reactions, where a chemical accepts a negative charge and falls apart to form a smaller chemical (Figure 3.1, Reactions 1 and 2),
2) photolysis, where photons decompose or ionize chemicals (Figure 3.1, Reactions 3-6),
3) neutral + neutral association reactions, defined as $A + B \rightarrow C + D$ (Figure 3.1, Reactions 7-10),
4) neutral + Ion association reactions, defined as $A + B^{+/-} \rightarrow C + D^{+/-}$ (Figure 3.1, Reactions 11-16),
5) gas-grain adsorption and desorption, assuming desorption occurs 10% of the time (Garrod (2013), Figure 3.1 , Processes 17-20).

Four types of photons were included in the model for photolysis reactions. Photons produced by the UV flux (γ_{UV}); Lyα photons (γ_{Ly_α}), which can carry up to 75% of the UV flux (Fogel et al., 2011); X-ray photons produced by the flux and flares; photons ($\gamma_{UV,fl}$) produced by the X-ray field, which result in H_2 fluorescence of UV photons that interact with other compounds in the disk, including H_2O.

3.2 Methods

A total of 20 points along the disk were tested with radii of $R = 1, 5, 10$, and 20 AU and normalized vertical heights of $Z/R = 0.0, 0.1, 0.2, 0.3$, and 0.4. See red points in Figure 2.2 . These points were chosen since they are are relatively close (compared to the total radius of the disk) to the star, and the vertical heights allow us to observe responses in the different vertical regions of the disk. We additionally explored models at 50 AU and saw relatively little change as discussed below in Section §4. The cosmic ray rate

was held constant at 2.0×10^{-20} ionizations per H_2 per second. However, Cleeves et al. (2013) determined that cosmic rays are energetically negligible compared to X-rays above

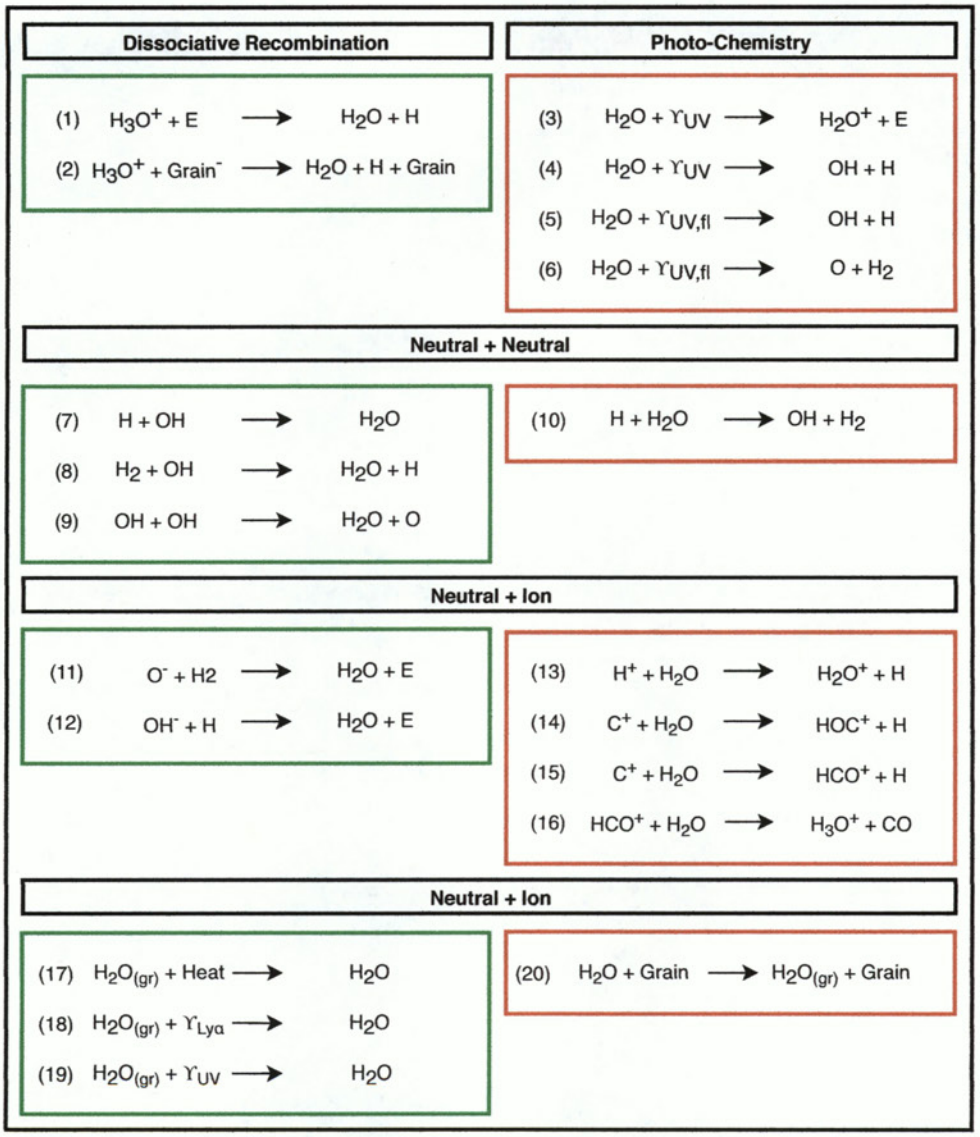

FIGURE 3.1 20 processes contributing to the production and consumption of *gaseous* H_2O. $H_2O_{(gr)}$ is ice water adsorbed onto grain particles. E is an electron, γ_{UV} are UV photons produced by the UV flux, $\gamma_{UV,fl}$ are UV photons released by H_2 fluorescence cause by X-ray photons, and $\gamma_{Ly\alpha}$ are UV photons that can carry up to 75% of the UV flux (Fogel et al., 2011). A dissociative recombination reaction occurs when a particle accepts a negative charge, then falls apart into a smaller particle. In this case, H_3O^+ falls apart into H_2O. Photochemistry occurs when a photon causes a chemical reaction to occur. Neutral + neutral reactions occur when two neutral species combine to form a new species or set of new species. Neutral + ion reactions occur when a neutral species reacts with a charged species to form a new species or set of species. Adsorption and desorption processes do not involve a chemical change, but are the physical processes of water freezing and desorbing on grain particles.

the mid-plane, the region modeled in this paper, and so the specific value of this input parameter does not impact our findings. See Appendix, Table 7.1 for physical values at all twenty points. Changes in chemical abundance per H atom are determined by plotting $\Delta\chi$, which represents the relative change in abundance compared to a model with no X-ray flares, versus time and is defined as:

$$\Delta\chi = \frac{\Delta\chi_{\text{withflare}}}{\Delta\chi_{\text{withoutflare}}}$$

It should be noted that highly abundant ($\geq 10^{-5}$) chemicals do not show change as strongly as chemicals with low abundances (10^{-20}). Individually, these points show H_2O response at one point in the disk, but together they create a 2D model mapping out H_2O flare responses at representative R and Z/R values shown in Figure 4.1.

X-ray flare strength was 100 times the magnitude of the normal X-ray luminosity, which was $L_{\text{XR}} = 4 \times 10^{30}$ erg s^{-1}. The flare rise time is 3.0 hours, and decay time is 5.0 hours. These timescales are chosen to be typical of observed X-ray flares from T-Tauri stars (e.g., Preibisch & Feigelson (2005)). We ran models for two different types of X-ray flares. Test 1 was run with a flare at 0.5 Myr ($t = 0$ days); Test 2 was run with two flares in rapid succession at 0 days and 10 days.

CHAPTER 4

Results

To guide the discussion in the following Sections key H_2O reactions and processes at the twenty points of the disk have been compiled and and numbered in Figure 3.1 . The following Sections will refer back to these processes.

4.1 Physical Trends in the Disk

The model revealed that H_2O responses beyond 20 AU are insignificant compared to distances interior to 20 AU. At distances greater than 20 AU there are X-ray flare responses, but responses are typically $\leq$ 7%, and the H_2O abundance is $\leq 10^{-9}$ at most points. This suggests that that the impact of X-ray flares on H_2O is diluted.

Figure 4.2 shows H_2O responses at 20 points on the disk. Several trends are seen in response patterns. The mid-plane is observed along $Z/R = 0$, where there is no flare response. Photons scatter in the PDR and warm molecular layer before reaching the mid-plane, so no response is expected.

The impact of X-rays was observed to be dependent on radial distance and density shielding across the entire grid. Response strength decreases from the inner disk atmosphere to the outer disk atmosphere. This shows that with increasing radii response decreases, and responses are lower in high density regions such as the mid-plane.

The snow line, the point at which H_2O exists primarily in the solid rather than *gaseous* state, can also be seen by finding drops in initial H_2O abundances across the disk. Any points where *gaseous* H_2O abundance is less than 10^{-5} falls in the snow line, where $H_2O_{(gr)}$ is more dominant than gas-phase H_2O. Abundance at $(R, Z/R) = (1.0\,\mathrm{AU}, 0.4)$ is an exception, since this region is strongly impacted by radiation from the star and *gaseous* H_2O does not exist in high abundance due to the high levels of radiation.

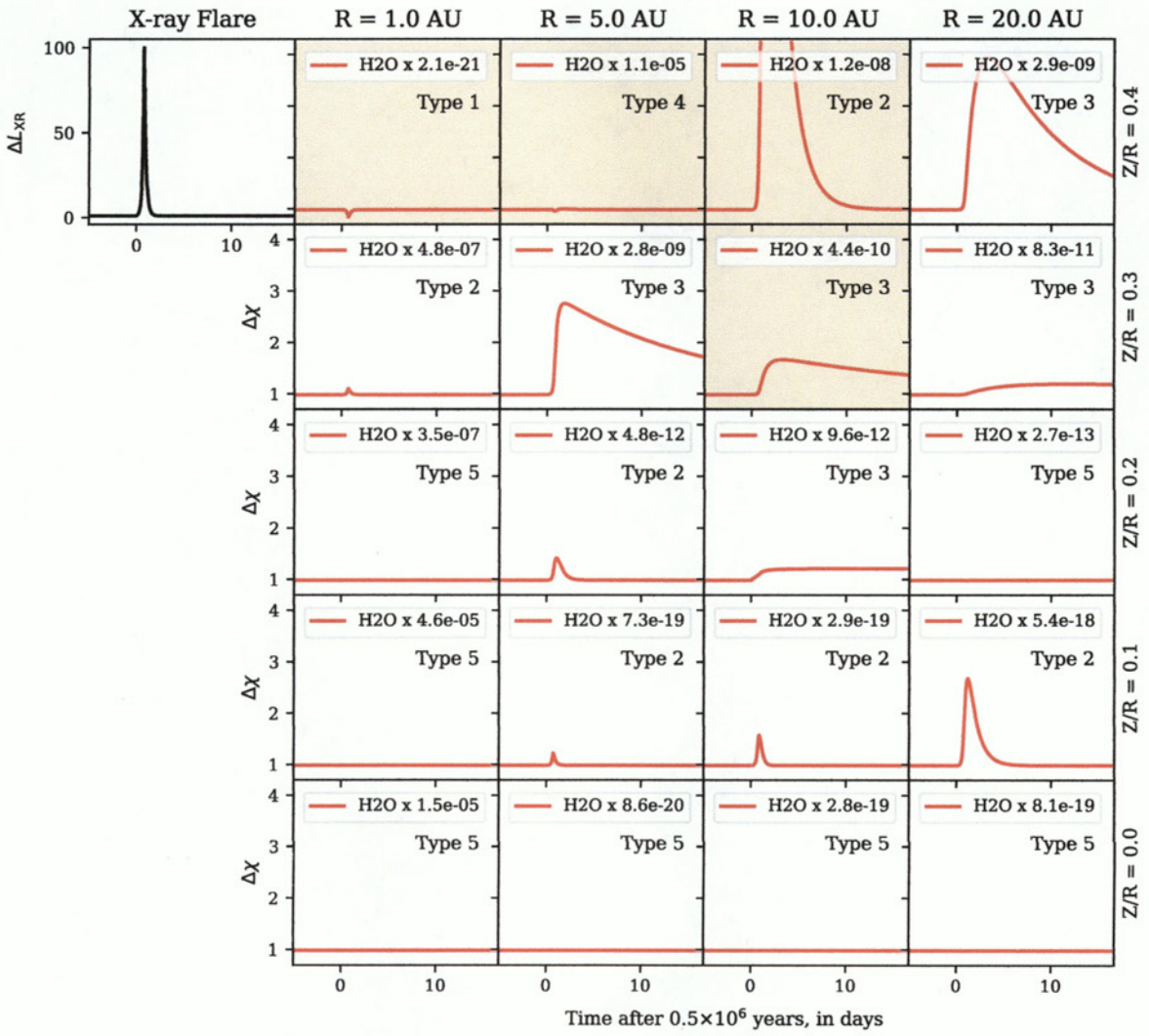

FIGURE 4.1 H_2O response grid from Test 1. See Chapter 3 Model and Methods for test parameters. Initial H_2O abundances appear at the top of each plot. For radii > 1AU H_2O exists dominantly in solid phase. Five types of curves are observed as discussed in Section 4.2. Analysis is presented in Section 4.2 Analysis of Different H_2O Response Curves.

4.2 Analysis of Different H_2O Response Curves

Five types of curves are observed in the disk. All twenty positions are labeled with their closest response curve type in Figure 4.1.

1) Net decrease, such as $(R, Z/R) = (1.0\,\mathrm{AU}, 0.4)$, where the response curve is a negative spike,
2) net production with fast rise and decay ($t < 5$ days), such as $(R, Z/R) = (10.0\,\mathrm{AU}, 0.4)$, where the response curve is a positive spike,
3) net production with long term increase ($t > 5$ days), such as $(R, Z/R) = (10.0\,\mathrm{AU}, 0.3)$, where the curve increases and experiences an exponential decay,
4) hybrid, such as $(R, Z/R) = (5.0\,\mathrm{AU}, 0.4)$, where the curve decreases to a minimum below the initial abundance then increases to a maximum spike,
5) no flare response.

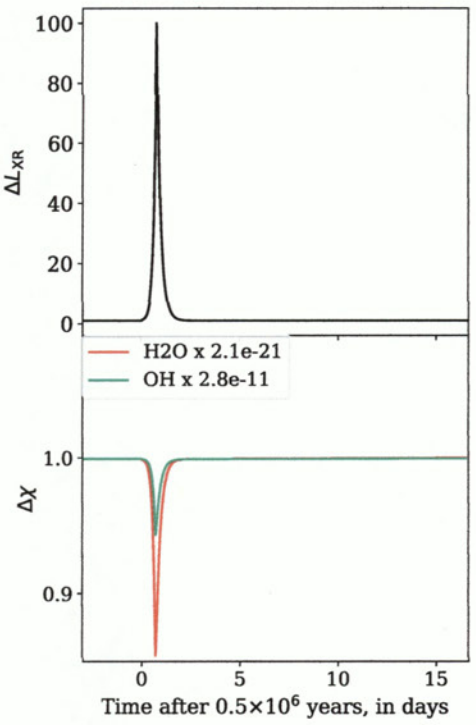

FIGURE 4.2 Type 1 Reaction Curve: Net Destruction, $(R, Z/R) = (1.0\,\mathrm{AU}, 0.4)$. H_2O is destroyed though photolysis to produce OH (Reaction 4), but H_2O is reformed by Reactions 7 and 8 to return to its initial abundance. OH abundance decreases due to rapid photolysis.

Curve types are further analyzed in this Section. The seven fastest processes involved in the production and destruction of *gaseous* H_2O are listed for each response type; processes are catalogued in Figure 3.1 . OH is also examined for Type 1 response curves, and 9 different reactions were observed and are also listed in Figure 3.1. In the following Tables negative rates indicate *gaseous* H_2O consumption, and positive rates indicate *gaseous* H_2O production. A net positive reaction rate indicates that the overall abundance of *gaseous* H_2O is increasing at that time, and a negative net reaction rate indicates that the overall abundance of *gaseous* H_2O is decreasing.

4.2.1 Type 1: Net Destruction

Only one point in the disk shows a net destruction curve, $(R, Z/R) = (1.0\,\mathrm{AU}, 0.4)$ shown in Figure 4.2. Water abundance drops 15% after 0.75 days, then quickly increases to approximately its initial abundance.

TABLE 4.1 Type 1 H_2O Related Processes

Reaction Number	0 days Initial	Reaction Number	0.75 days Minimum	Reaction Number	3 days levels out
4	-17.7	4	-15.1	4	-17.7
8	13.7	8	13.0	8	13.7
7	4.21	7	3.98	7	4.21
3	-1.13	11	1.32	11	1.33
10	-0.739	3	-0.968	3	-1.13
11	1.32	6	0.920	10	-0.739
9	0.187	5	-0.920	9	0.187
Net Rate	-4E-22		7.4E-21		1.4E-21

Rates are given in $\times 10^{-19}\text{cm}^{-3}\ \text{s}^{-1}$ for the net destruction curve at point $(R, Z/R) = (1.0\,\text{AU}, 0.4)$. Negative rates indicate consumption. Positive rates indicate production. Reactions and processes are catalogued in Figure 3.1.

Detailed rates for processes involving H_2O are evaluated at 3 representative times, before ($t = 0$ days), during ($t = 0.75$ days), and after ($t = 3$ days) the X-ray flare. Table 4.1 shows the seven fastest processes at each of these key times. Of all the disk points modelled, this one is the closest to the star with the largest vertical height. This point is impacted by photons from the X-ray flare much more strongly than other points on the disk. This can be seen by the appearance of Reactions 5 and 6 in Table 4.1 at $t = 0.75$ days. These two reactions involve the H_2O destruction by UV photons that arise from X-ray photon induced H_2 fluorescence. At $t = 0$ days and $t = 3$ days Reactions 5 and 6 are not among the seven fastest processes. They only appear during the time of the flare.

OH abundance was expected to increase since it is a product of Reactions 4 and 5: however, Figure 4.2 shows that OH abundance decreases. There are two explanations as to why. First, Reactions 4 and 5 are not among the seven fastest OH reactions, so it is likely that they do not strongly

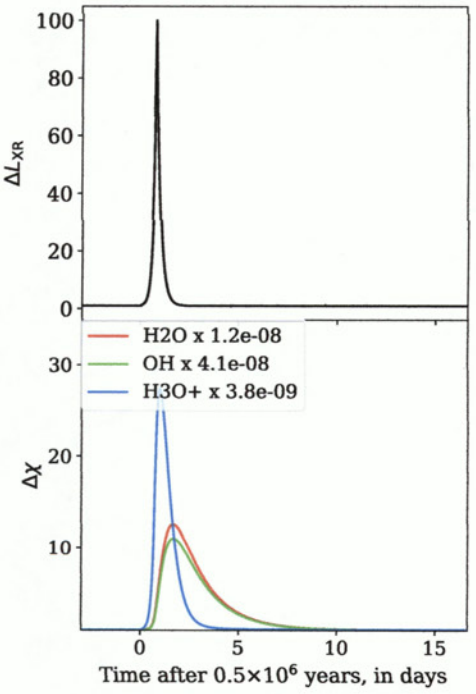

FIGURE 4.3 Type 2: Net Production with Fast Rise and Decay (< 5 days), $(R, Z/R) = (10.0\,\text{AU}, 0.4)$. Dominant H_2O production is dissociative recombination of H_3O^+ (Process 1) and OH combination with H_2 (Process 8). Dominant H_2O consumption is photolysis (Process 4).

impact OH as they do H_2O. In addition, OH experiences multiple destructive photolysis reactions, including OH ionization and dissociation to form O and H that result in a negative net rate of -3.47×10^{-11} at 0.77 days.

4.2.2 Type 2: Net Production with Fast Decay (< 14 days)

Type 2 Rates are given in reaction curves, a net production with fast rise and decay, occur commonly in the disk grid (Figure 4.1); the strongest response is at $(R, Z/R) = (10.0\,\mathrm{AU}, 0.4)$, shown in Figure 4.3. At this point H_2O abundance increases 1300% at 2.35 days, then returns back to its initial abundance after 10 days.

Detailed rates are evaluated at four representative times, before ($t = 0$ days), during ($t = 2.35$ days and $t = 5$ days), and after ($t = 14$ days) the flare. Table 4.2 shows the seven fastest processes at each of these times. This point is both on the surface layer of the disk and radially close enough to feel a strong impact from the X-ray flare. Because of this, the photolysis of water rates increases during the time of the flare (particularly Reaction 4).

Figure 4.3 reveals that H_3O^+ abundance increases by over 2800% in direct response to the flare, which then speeds up the dissociative recombination of H_3O^+, which in turn drastically increases the production of H_2O. There is a flare response delay from H_2O because it takes time for H_3O^+ to find electrons to form H_2O.

Once H_3O^+ is consumed back to its initial abundance, Reaction 1 rate significantly drops $t = 5$ days, which drastically decreases H_2O production. Consumption is much faster than production (net rate $= -276 \times 10^{-7}\mathrm{cm}^{-3}\ \mathrm{s}^{-1}$) since H_3O^+ is no longer overly abundant to produce H_2O. The main destructive processes appear to be photolysis (specifically Reaction 4), and once H_2O abundance has returned to its initial abundance

TABLE 4.2 Type 2 H_2O Related Processes

Reaction Number	0 days Initial	2.35 days Maximum	5 days Decay	14 days Levels Off
4	-144	-1520	-415	-145
1	113	446	120	113
8	48.8	463	133	49.3
3	-9.21	-97.6	-26.5	-9.29
14	-5.76	-60.5	-16.1	-5.62
15	-2.85	-29.9	-7.97	-2.78
Net Rate	-0.03	-806	-213	-4.19

Rates are given in $\times 10^{-7}\mathrm{cm}^{-3}\ \mathrm{s}^{-1}$ for net production with fast rise and fast decay curve at $(R, Z/R) = (10.0\,\mathrm{AU}, 0.4)$. Negative rates indicate consumption. Positive rates indicate production. Reactions and processes are catalogued in Figure 3.1.

the pseudo steady state equilibrium is reached and further changes in abundance do not occur.

4.2.3 Type 3: Net Production with Long Term Increase (> 14 days)

Response curves that experience a net production with a long term (> 14 days) increase are observed along the $Z/R = 0.3$ and $Z/R = 0.2$ vertical heights (Figure 3.1). The point $(R, Z/R) = (10.0\,\mathrm{AU}, 0.3)$ was chosen to represent this trend, and whose evolution in plotted in more detail in Figure 4.4. After a 0.2 day delay, H_2O increases 68% at 3.3 days, then steadily decreases until the end of the 15.5 day run. Detailed rates are evaluated at four representative times, before ($t = 0$ days), during ($t = 1.25$ days and $t = 4.35$ days), and after ($t = 8$ days) the X-flare. Table 4.3 shows the seven fastest processes at each of these key times.

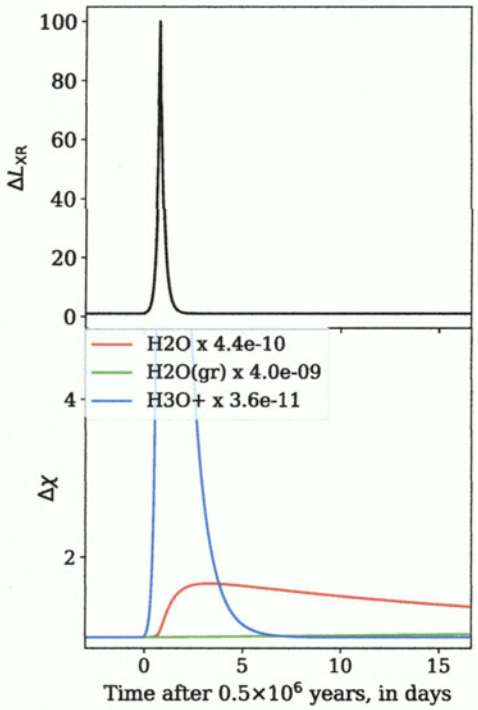

FIGURE 4.4 Type 3: Net Production with Long Term (> 14 days) Increase $(R, Z/R) = (10.0\,\mathrm{AU}, 0.3)$. Main H_2O production is dissociative recombination of H_3O^+ (Reactions 1 and 2). Main H_2O consumption is adsorption (Process 20). H_3O^+ maximum is $\Delta\chi = 21.7$.

Like a Type 2 response (§4.2.2), the initial increase in H_2O abundance is caused by a sharp increase in H_3O^+ abundance (Figure 4.2.3 shows that H_3O^+ abundance increases over 2170%. H_3O^+ undergoes dissociative recombination via Reactions 1 and 2 to produce H_2O faster than H_2O is consumed (Table 4.3 at 1.25 days). While photolysis does occur, this point is partially shielded from the destructive photons, so the most contributing H_2O consumption process is freezing. Due to the weaker UV field radiation, *gaseous* H_2O is not quickly consumed, so there is an exponential tail to the curve as H_2O slowly freezes onto grains as ice (Process 20). Figure 4.2.3 shows that $H_2O_{(gr)}$ is steadily increasing (to $\sim 4\%$) as H_2O is steadily decreasing. It is to be noted that H_2O decline appears greater than $H_2O_{(gr)}$ increase for two reasons. First, $H_2O_{(gr)}$ is more abundant than H_2O, so the change in abundance is smaller, and second, H_2O is also being consumed via multiple processes including slow UV destruction, so not all consumed *gaseous* H_2O is being converted to ice H_2O.

TABLE 4.3 Type 3 H_2O Related Reactoins

Reaction Number	0 days Initial	1.25 days Increasing	4.35 days Maximum	8 days Decrease
20	-16.5	-25.2	-27.4	-25.9
1	8.35	223	11.6	8.42
19	4.02	4.02	4.06	4.10
18	4.02	4.02	4.06	4.10
4	-2.02	-2.76	-3.36	-3.17
11	1.34	1.96	1.37	1.34
2	0.941	17.1	1.28	0.945
Net Rate	6.30E-10	2.24E-5	-8.69	-10.4

Rates are given in $\times 10^{-7}$cm^{-3} s^{-1} for the net production with exponential decay curve at point $(R, Z/R) = (10.0\,\mathrm{AU}, 0.3)$. Negative rates indicate consumption. Positive rates indicate production. Reactions and processes are catalogued in Figure 3.1.

4.2.4 Type 4: Hybrid

Unlike the other curve types, the hybridized response experiences both an absolute minimum and an absolution maximum. $(R, Z/R) = (5.0\,\mathrm{AU}, 0.4)$ is the only hybrid response observed in this model (Figure 4.5). H_2O abundance initially decreases ~3% at $t = 0.5$ days, then increases $\sim$ 1% above initial abundance at $t = 1.7$ days, then returns back to its initial abundance for the duration of the test (15 days) Detailed rates are evaluated at four representative times, before ($t = 0$ days), during ($t = 0.5$ days and $t = 1.7$ days), and after ($t = 5$ days) the flare. Table 4.4 shows the seven fastest processes at each time.

Similar to the Type 1 response at $(R, Z/R) = (1.0\,AU, 0.4)$ (§4.2.1), this point is strongly impacted by the flare since it is at a close distance to the star (5.0 AU) and on the disk surface. However, it is far enough away from the star to have a high abundance of *gaseous* molecules and ions, such as H_2O and $H_3O^+ (\geq 10^{-6})$ Because of this its proximity to the star and high

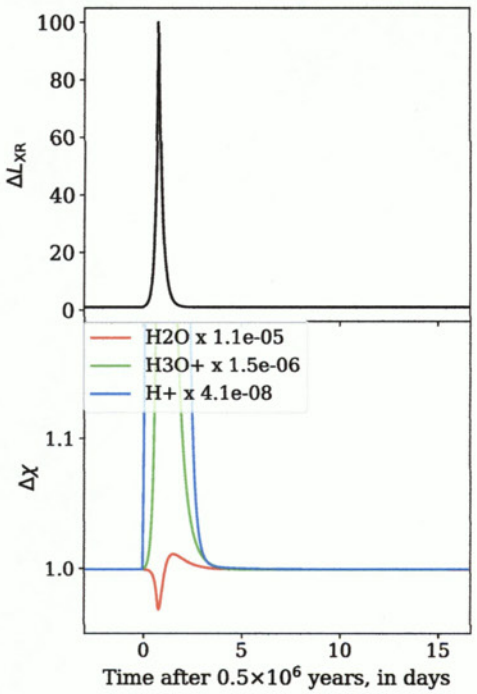

FIGURE 4.5 Type 4: Hybrid, $(R, Z/R) = (5.0\,\mathrm{AU}, 0.4)$. Initially, H_2O is consumed by an increase in photolysis reactions (Processes 5 and 6), then is produced by dissociative recombination of H_3O^+ (Process 1), then it is consumed by a combination of photolysis (Proceses 4, 5, and 6) and ionization (Process 13) to return to its initial abundance.

TABLE 4.4 Type 4 H_2O Related Processes

Reaction Number	0 days Initial	0.5 days 1^{st} Decay	1.1 days Growth	1.7 days 2^{nd} Decay	5 days Level Off
8	253	252	249	253	253
4	-244	-243	-243	-247	-244
3	-15.6	-15.6	-15.6	-15.8	-15.6
1	6.55	7.95	21.3	9.23	6.56
6	-0.122	-1.75	-2.32	-0.247	-0.122
5	-0.122	-1.75	-2.32	-0.247	-0.122
13	-0.058	-0.385	-2.15	-0.291	-0.058
Net Rate	0.523	-1.83	5.47	-0.524	0.532

Rates are given in $\times 10^{-4} \mathrm{cm}^{-3}\ \mathrm{s}^{-1}$ for the net production with fast rise and fast decay curve at point $(R, Z/R) = (5.0\,\mathrm{AU}, 0.4)$. Negative rates indicate consumption. Positive rates indicate production. Reactions and processes are catalogued in Figure 3.1.

abundance, H_2O flare response with a combination of Type 1 (§4.2.1) and Type 2 (§4.2.2) curves.

During the initial flare impact, H_2O abundance decreases due to an increase photodissociation (Processes 5 and 6), similar to Type 1. After the initial impact, H_2O is then produced by dissociative recombination of H_3O^+, similar to Type 2. A delay in increased water abundance is also observed at $(R, Z/R) = (10.0\,AU, 0.4)$ (Figure 4.3) and $(10.0\,AU, 0.3)$ (Figure 4.4). An initial decrease in H_2O abundance is only observed at $(R, Z/R) = (5.0\,\mathrm{AU}, 0.4)$ due to a greater flare impact. At the end of the flare H_2O is no longer being produced by Process 1 as quickly, since H_3O^+ abundance decreases (Figure 4.5). H_2O then returns to its initial abundance due to a combination of photolysis and ionization by H^+(Process 13). The large increase in H^+ is produced by X-ray photons removing an electron from H atom.

4.2.5 Type 5: No Response

Flare responses do not occur at the most dense regions of the disk ($\rho \geq 10^{-12}\,\mathrm{g\,cm^{-3}}$) or along the mid-plane for two reasons. One, there is a large abundance of *gaseous* H_2O in these regions ($\geq 10^{-7}$), so H_2O is not as sensitive to change. Two, there is a low X-ray ionization rate (essentially zero), so there are fewer X-ray photons present to cause a response.

4.3 Response Trends in the Disk

By comparing the vertical and horizontal response trends in the disk with the five curve types discussed in the previous Section (§4.2) general reaction trends across the disk can be found.

Response Types 2-4 show that the main H_2O production process is dissociative recombination of H_3O^+ (Reactions 1 and 2), which is produced from H_3^+ produced directly from the flare. Types 1-3 show that the main H_2O consumption processes are adsorption onto grains (Process 20) and photodissociation of H_2O (Reactions 3-6), both from photons produced by the UV flux and photons produced by H_2 fluorescence.

Along the vertical height traced by $Z/R = 0$ no response is observed. This height is along the mid-plane, and it is very difficult for photons to penetrate since they are scattered in the upper layers, so the X-ray ionization rate is very low ($\leq 10^{-27}\,\mathrm{s}^{-1}\mathrm{H}_2^{-1}$).

Along the vertical height traced by $Z/R = 0.1$, response curves behave with a Type 2 pattern, and water response increases with increasing radial distance. This is directly related to density. At shorter radii, such as $R = 1\,\mathrm{AU}$, the density is higher, and any molecules in this region are protected by the dense layers between the point and the surface of the disk. A second trend occurs along this vertical height: as radius increases the response curves begin to develop an lagging tail. This is likely because photon intensity decreases as distance from the star increases, so after the initial H_2O spike from Reactions 1 and 2, photons are not as abundant for destruction.

Along the vertical height traced by $Z/R = 0.2$, response curves vary in type. At $R = 1.0\,\mathrm{AU}$ there is no response since this point resides within a high dense region ($10^{-12}\,\mathrm{g\,cm}^{-3}$) where photons cannot penetrate. At $R = 5.0\,\mathrm{AU}$ density has dropped ($10^{-16}\,\mathrm{g\,cm}^{-3}$) to where photons can enter the region and cause an increase in H_3O^+, therefore leading to an increase in H_2O. At $R = 10.0\,\mathrm{AU}$ the region is still close enough to experience an increase in H_3O^+ abundance from the flare, but not close enough to feel the destructive impact of the photons. The temperature has also dropped enough so that *gaseous* H_2O more readily freezes onto grains. At $R = 20.0\,\mathrm{AU}$ the region is far enough from the star no response is observed.

Along the vertical traced by $Z/R = 0.3$, response curves are dominantly Type 3, net production with long term ($> 14\,\mathrm{days}$), curves. The point at $R = 1.0\,\mathrm{AU}$ does not experience an exponential decay as the other points in this vertical height since it is close enough to the star to feel the highly destructive photons. As radial distance increases the exponential tail elongates since destructive photon intensity decreases with decreasing UV flux.

Along the vertical height traced by $Z/R = 0.4$, response curves vary in type. At $R = 1.0\,\mathrm{AU}$ the region is close to the surface layer of the disk and close to the star,

so destructive photolysis is the most dominant reaction. As radial distance increases, the destructive capabilities of the photons decrease with decreasing X-ray ionization rate; at $R = 5.0$ AU both destruction and production occur; at $R = 10.0$ AU production via Reactions 1 and 2 is dominant over photolysis; $R = 20.0$ AU the curve likely follows the same behavior patterns listed for a Type 3 curve (§4.2.3).

4.4 Ice H_2O Responses

It is of interest to quantify how much of the gas phase response is imparted into the ice. $H_2O_{(gr)}$ responses discussed in this Section are obtained from Test 1. There is no flare response along the $Z/R = 0.2$ vertical height and below. Solid H_2O has the same relative response types as *gaseous* H_2O at radial distances of $R = 1.0$ and 5.0 AU, and along the disk surface at $R = 10.0$ and 20.0 AU. $H_2O_{(gr)}$abundance changes proportionally, but at a lesser degree, with *gaseous* H_2O abundance. This suggests that as excess H_2O is produced, H_2O adsorbs onto grains to form $H_2O_{(gr)}$ (Process 20). Once the excess H_2O returns back to its initial abundance, $H_2O_{(gr)}$ desorbs from the grain to return to a gas (Processes 17-19). Adsorption is observed in the rate analysis (§4.2), and this would re-establish the pseudosteady-state equilibrium established in the model (§3.1). It is to

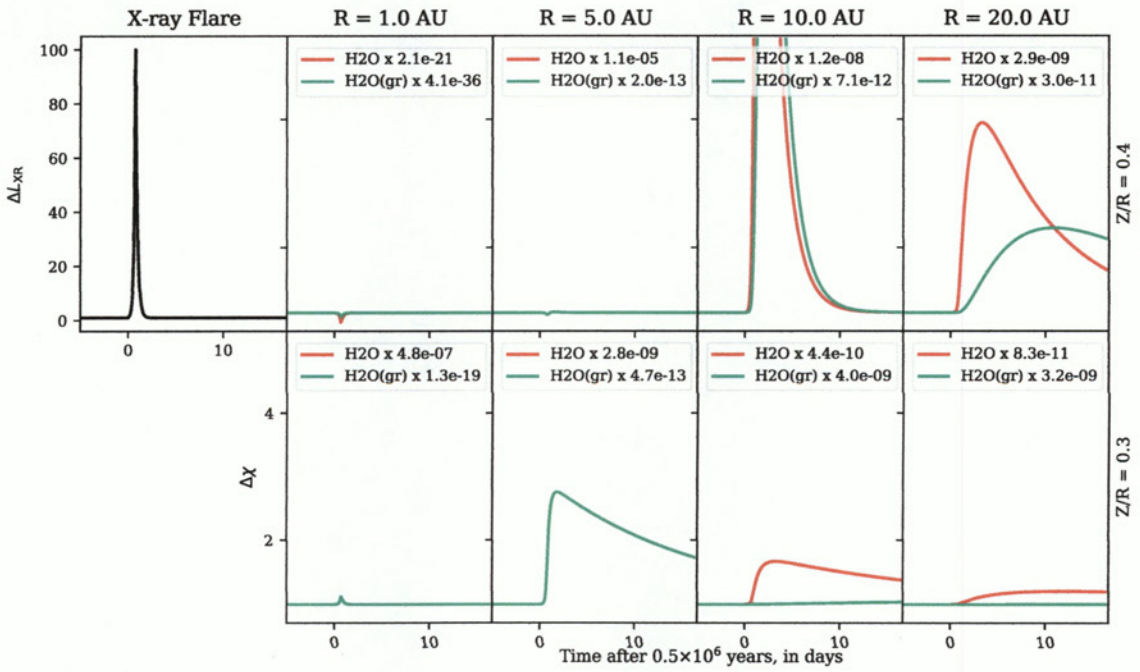

FIGURE 4.6 This plot shows *gaseous* H_2O and $H_2O_{(gr)}$ responses along the vertical height of $Z/R = 0.4$ and 0.3. $H_2O_{(gr)}$ has a similar response pattern to *gaseous* H_2O at all but one point, $(R, Z/R) = (10.0\,AU, 0.4)$. At this point *gaseous* H_2O appears to adsorb onto grains to increase $H_2O_{(gr)}$ abundance. As the mid-plane is approached $H_2O_{(gr)}$ experiences either no flare response or the responses are insignificant.

be noted that $(R, Z/R) = (20.0\,\mathrm{AU}, 0.4)$ $H_2O_{(gr)}$ appears to follow a different trend than H_2O, however the colder temperatures at this point ($T_{dust} = 90.2\mathrm{K}, T_{gas} = 117.4\mathrm{K}$) allow $H_2O_{(gr)}$ to persist longer than at points radially closer to the star.

The point at $(R, Z/R) = (10.0\,\mathrm{AU}, 0.3)$ has an $H_2O_{(gr)}$ abundance that steadily increases to 3.8% of its initial abundance at the end of the test (17 days). The point at $(R, Z/R) = (20.0\,\mathrm{AU}, 0.3)$ steadily increases its $H_2O_{(gr)}$ abundance to 0.2% of the initial abundance at the end of the test (17 days). This behavior indicates that H_2O adsorption onto grains is significant at radial distances of 10 AU or greater at vertical heights near $Z/R = 0.3$.

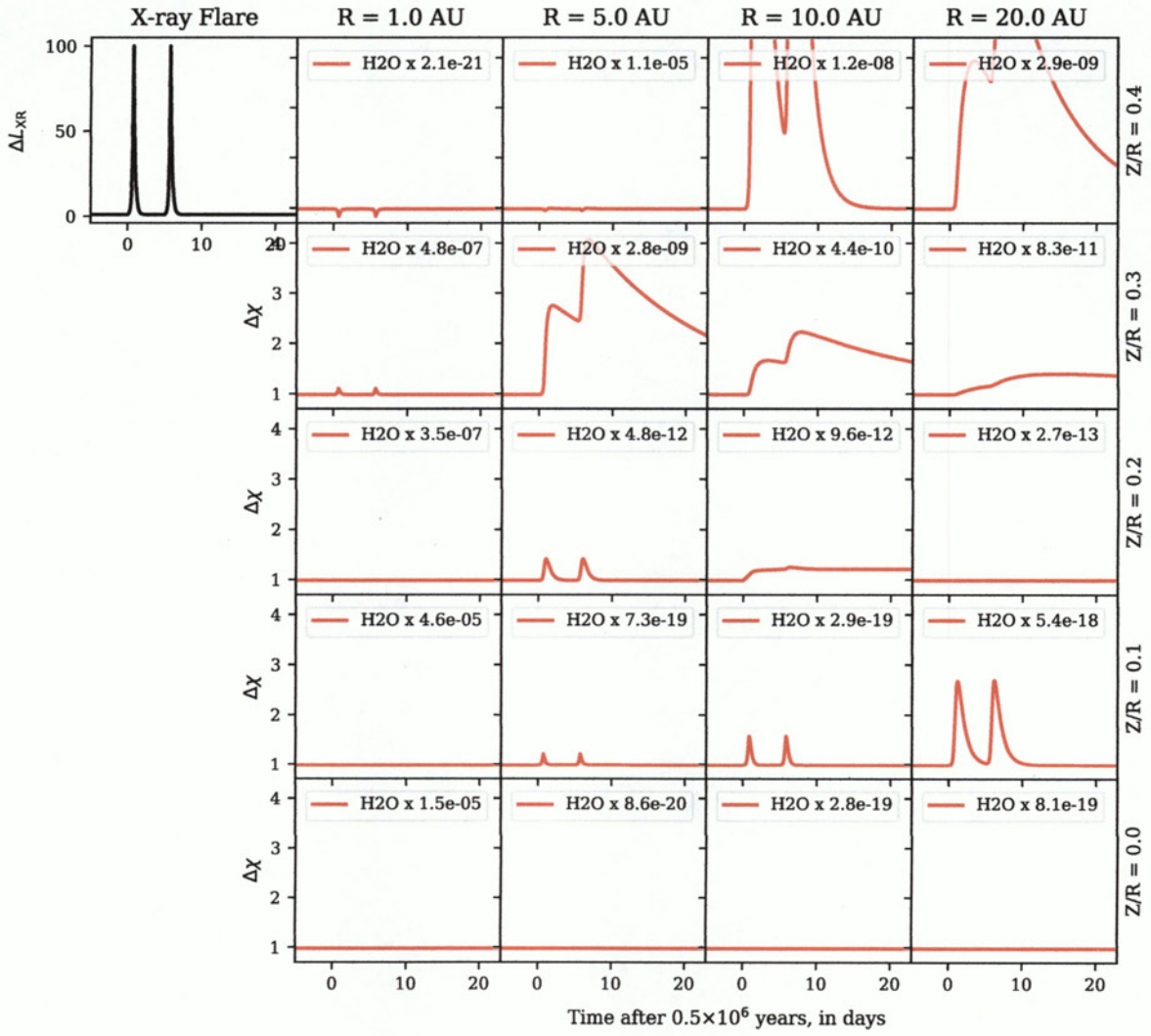

FIGURE 4.7 Test 2 grid. Test 2 is ran with the same parameters as Test 1, but is exposed to two X-ray flares instead of 1. Flares occur at $t = 0$ days and $t = 5$ days. (See §3.2 Methods for parameters).

4.5 Impacts of Muli-flare Events

In addition to the single flare analysis (Test 1), we have run a model that has multiple flaring events (Test 2) and discuss them qualitatively here. Between Tests 1 and 2 only slight variations occurred. As seen by comparing Figures 4.1 and 4.7, the plots have similar response patterns. Figure 4.7 shows that a response to two flares behaves in a similar pattern to a response to one flare, only the responses "stack up" on each other. This suggests that multiple flares will have a similar effect as a single flare, and their cumulative effect will be related to the timing between flares.

4.6 Flare Strength Variation

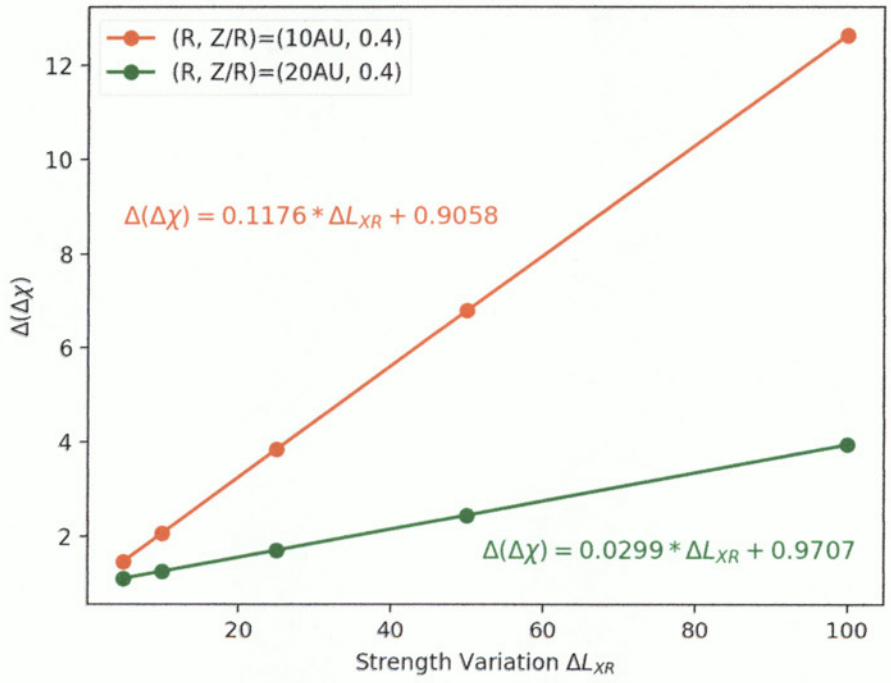

FIGURE 4.8 This plot shows the maximum change in H_2O abundance that occurs due to flare strengths of 100, 50, 25, 10, and 5. Δ ($\Delta\ \chi$) represents change of the change of abundance due to flaring. Red corresponds to the point $(R, Z/R) = (10\,AU, 0.4)$ and green corresponds to $(R, Z/R) = (20\,AU, 0.4)$. These two locations would be the most likely candidates for observations.

All previous analyses were performed with X-ray flare strengths equal to 100 times the background X-ray ionization rate, which is considered an extremely strong and rare flaring event (once every $\sim$ 3 to 4 years, Getman et al. (2008); Wolk et al. (2005)) We found that weaker flares ($\sim$ 5 times X-ray ionization rate), which are much more common, produced similar abundance profiles to flare strengths of 100 in this model, but with smaller

amplitude. See Appendix for H_2O responses to flares strengths of 5, 10, 25, and 50 along vertical heights $Z/R = 0.3$ and 0.4. These heights were chosen since they represented the locations that had the most significant change while also having abundant gas-phase water.. Figure 4.8 shows the maximum change in H_2O abundance that occurs due to flare strengths corresponding to a change in 100, 50, 25, 10, and 5 X-ray luminosity. Both $(R, Z/R) = (10\,AU, 0.4)$ and $(20\,AU, 0.4)$ were found to have a linear dependence on change in H_2O abundance compared to the change in X-ray luminosity. Maximum changes in H_2O responses at $(R, Z/R) = (10\,AU, 0.4)$ can be predicted using the equation $\Delta\chi = 0.1176 * \Delta L_{XR} + 0.9058$. The point $(R, Z/R) = (20\,AU, 0.4)$ can be predicted using the equation $\Delta\chi = 0.0299 * \Delta L_{XR} + 0.9707$, where ΔL_{XR} is the change in X-ray ionization rate during a flare with respect to the typical background X-ray ionization rate.

CHAPTER 5

Discussion

Rate analysis in the Results section showed that X-ray flares can induce an increase in H_3O^+ abundance, which then undergoes dissociative recombination reactions (1 and 2) to form H_2O. H_2O is then consumed via two main processes: photolysis (Reactions 3-6) and adsorption (Process 20) to return to its initial abundance typically after ~ 5 days. However, some points show that H_2O abundance can decrease or increase for tens of days, or longer (Type 3 responses). Each Type 3 H_2O response does return to its initial abundance within a year, with the exception of $(R, Z/R) = (10\,AU, 0.2)$. This point experiences a permanent 23% increase (> 1 yr).

In the following Sections we discuss which of these responses could be observed in the IM Lup protoplanetary disk. Ideally, observable H_2O abundances will be $\geq 10^{-10}$ and flare response will be $> 5\%$.

5.1 X-ray Ionization Rate and Density Relate to Flare Response Magnitude

The models show that H_2O will not respond to X-ray flares in regions where the X-ray ionization rate is $< 10^{-21}\,\mathrm{s}^{-1}\mathrm{H}_2^{-1}$, which occurs at densities $> 10^{-13}\,\mathrm{g\,cm}^{-3}$. These are noted as No Response Regions, and are represented by blue boxes in Figure 5.1. This region primarily corresponds to Type 5 response curves and includes all mid-plane points, points within the snow line, and points less than 5 AU from the star. It is to be noted that $(R, Z/R) = (5.0\,\mathrm{AU}, 0.1)$, $(10.0\,\mathrm{AU}, 0.1)$, and $(20\,\mathrm{AU}, 0.1)$ fall in this region and have flare responses. However, at these points *gaseous* H_2O abundance ($\leq 10^{-18}$) is among the lowest seen in the model (10^{-20}), so any change in H_2O abundance at these points will appear on the plots. These changes are considered minimal and fall into the No Response Region, because they likely cannot be observed.

When the X-ray ionization rate is $10^{-18}\,\mathrm{s}^{-1}\mathrm{H}_2^{-1}$ plus or minus an order of magnitude, and the density is $10^{-13}\,\mathrm{g\,cm}^{-3}$, H_2O abundance is between 10^{-13} and 10^{-12} per H atom. Regions with this ionization rate and density are noted as Radially Dependent Regions,

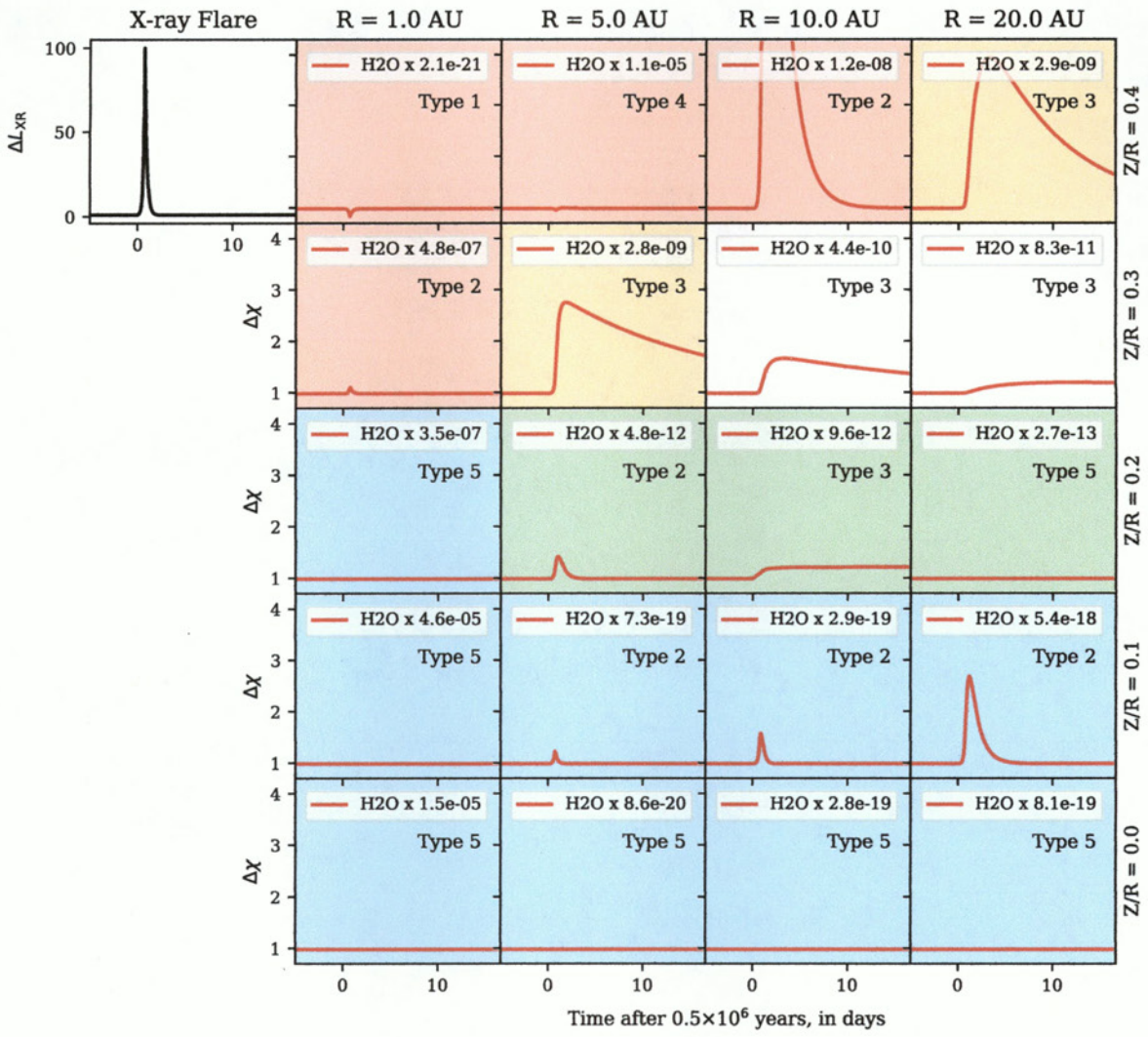

FIGURE 5.1 This is the old abundances The shown response curves are from Test 1. Blue boxes indicate that the point lays in a No Response Region (or that the response is not significant because abundance is $\leq 10^{-18}$), and the region has a density $> 10^{-13}\,\mathrm{g\,cm^{-3}}$and X-ray ionization rate $> 10^{-21}\,\mathrm{s^{-1}H_2^{-1}}$. Green boxes indicate a Radially Dependent Region, where density is $\sim 10^{-13}\,\mathrm{g\,cm^{-3}}$and X-ray ionization is $\sim 10^{-18}\,\mathrm{s^{-1}H_2^{-1}}$plus or minus an order of magnitude. Points that are not colored blue or green $(Z/R > 0.2)$ are High Response Regions, where density is $\leq 10^{-12}\,\mathrm{g\,cm^{-3}}$and X-ray ionization rate is $\geq 10^{-17}\,\mathrm{s^{-1}H_2^{-1}}$. Red boxes indicate Dominant Photolysis Consumption Regions, where both $\mathrm{T_{gas}}$ and $\mathrm{T_{dust}}$ are above 160 K and the UV flux is $\geq 10^{12}\,\gamma\mathrm{s^{-1}cm^{-2}}$. Orange boxes indicate Photolysis and Adsorption Regions, where $100\,\mathrm{K} < \mathrm{T_{gas}} < 160\,\mathrm{K}$, $80\,\mathrm{K} < \mathrm{T_{dust}} < 120\,\mathrm{K}$, and the UV flux is $\sim 10^{11}\,\gamma\mathrm{s^{-1}cm^{-2}}$. Points not colored red or orange indicate Dominant Adsorption Regions, where both $\mathrm{T_{gas}}$ and $\mathrm{T_{dust}}$ are below 100 K, and the UV flux is $\leq 10^{11}\,\gamma\mathrm{s^{-1}cm^{-2}}$.

where they are likely to have a flare response if they are interior to 20 AU of the star, but at radii at and beyond 20 AU there will likely be no flare response. These regions are represented by green boxes in Figure 5.1. Due to their low abundances, Radially

Dependent Regions likely cannot be observed.

Regions with X-ray ionization rates $\geq 10^{-17}\,\mathrm{s}^{-1}\mathrm{H}_2^{-1}$ and in density regions $\leq 10^{-12}\,\mathrm{g\,cm}^{-3}$ are defined as High Response Regions. When X-ray ionization rate is $\geq 10^{-10}\,\mathrm{s}^{-1}\mathrm{H}_2^{-1}$ Type 1 response curves are observed. High Response Regions in Figure 5.1 are any points without a blue or green box. *Gaseous* H_2O abundance is $\geq 10^{-11}$ and X-ray flare response is $\geq 10\%$. The point $(R, R/Z) = (1\,\mathrm{AU}, 0.4)$ is an exception. H_2O abundance is much too low (10^{-21}) at this point, but it falls in the High Response Region due to its high X-ray ionization rate ($10^{-10}\,\mathrm{s}^{-1}\mathrm{H}_2^{-1}$). High Response Regions near the surface of the disk ($Z/R \geq 0.3$) and between 5 AU and 20 AU distance from the star are the most promising regions for observation.

5.2 Relationship Between UV Flux and Temperature to Photolysis or Adsorption Consumption of H_2O

Within High Response Regions *gaseous* H_2O consumption was found to occur largely via photolysis (Reactions 3-6) and adsorption (Process 20) onto grains. The dominant consumption process is determined by UV flux and gas and dust temperature.

Photolysis is dominant where both gas and dust temperature are $> 160\,\mathrm{K}$, and the UV flux is $\geq 10^{12}\,\gamma\mathrm{s}^{-1}\mathrm{cm}^{-2}$. They tend to occupy the surface of the disk where there is photons are more readily available and the temperatures are warmer ($\mathrm{T_{gas}}$ can reach hundreds to thousands K). Photolysis regions are represented by red boxes in Figure 5.1.

When the UV flux is $\sim 10^{11}\,\gamma\mathrm{s}^{-1}\mathrm{cm}^{-2}$, $100\,\mathrm{K} < \mathrm{T_{gas}} < 160\,\mathrm{K}$, and $80\,\mathrm{K} < \mathrm{T_{dust}} < 120\,\mathrm{K}$ both photolysis and adsorption occur. The two points modeling this region are either (1) near, but not on ($Z/R = 0.3$) on the surface of the disk and is 5 AU from the star, or (2) on the surface of the disk ($Z/R = 0.4$) but radially far (20 AU) from the star. Regions that are dominated by both photolysis and adsorption are represented by orange boxes in Figure 5.1.

When both $\mathrm{T_{dust}}$ and $\mathrm{T_{gas}}$ drop below 100 K and UV flux is $< 10^{11}\,\gamma\mathrm{s}^{-1}\mathrm{cm}^{-2}$adsorption onto grains is the dominant consumption process. The model suggests that when the UV flux is between $10^{9}\,\gamma\mathrm{s}^{-1}\mathrm{cm}^{-2}$ and $10^{11}\,\gamma\mathrm{s}^{-1}\mathrm{cm}^{-2}$ and the temperature is between 80 K and 100 K freezing takes tens of days to return *gaseous* H_2O to its abundance after the X-ray flare. These specific conditions correspond to Type 3 response curves. Adsorption dominated processes are any points without a red or orange box in Figure 5.1.

5.3 Future Goals

Future goals for this project include exploring weaker X-ray flare strengths that more accurately model X-rays observed in the IM Lup protoplanetary disk. Other goals include

an in depth rate analysis on H_3O^+ to better understand its formation from the flare, or running a long test (up to year or longer) through the model to see if chemical abundances are affected on a scale longer than a few days. Molecules and ions other that H_2O, such as carbon chains or any ion dependent chemicals likely to be affected by an X-ray flare.

Observational goals include obtaining spectroscopic data from the James Webb Telescope (JWST) after its launch in October 2018, or Atacama Large Millimeter/submillimeter Array (ALMA). JWST's ability to monitor the near infrared will be ideal for identifying molecules such as H_2O, in radial distance close to the star (within 10 AU). ALMA's ability to observe submillimeter emission will be ideal for identifying molecules in larger radial distances (such as between 10 to 100s of AU).

CHAPTER 6

Summary

This project determined that *gaseous* H_2O in a protoplanetary disk surrounding a T-Tauri star can respond to X-ray flares in many ways, but the effects are typically short-time (days).

Analyzing the chemical reaction rates in detail reveals that H_2O production occurs dominantly by dissociative recombination of H_3O^+, and H_2O consumption occurs dominantly by photolysis or adsorption onto grains. Photolysis is dominant in the warmer ($T > 160\,K$) upper layers of the disk, whereas adsorption is dominant in cooler ($T < 100\,K$) deeper layers of the disk. Response magnitude is dependent on the region's X-ray ionization rate and density. Regions of low density have high X-ray ionization rates, which tend to have large *gaseous* H_2O abundances and flare responses. Regions with high density of low X-ray ionization rates, which tend to have low *gaseous* H_2O abundances either no flare response or no observable flare response.

H_2O abundance returns to its initial abundance at all but one of the twenty tested points within one year due to the following generalized process. (1) X-ray photons emitted from the flare ionize H_2 to H^+. (2) H^+ fluoresces to emit UV photons ($\gamma_{UV,fl}$). (3) $\gamma_{UV,fl}$ γ_{UV} and photolyze H_2O (Reactions 3-6). This increases the amount of H_2O^+ abundance (Reaction 3). (4) H_2O^+ forms H_3O^+ via the following process: (5) H_3O^+ undergoes dissociative recombination to form H_2O (Reactions 1 and 2).

It is to be noted that the other processes listed in Figure 3.1 are also key in changes in H_2O abundance due to X-ray flaring. However, the listed process above is an explanation for why H_2O abundance consistently returns back to its initial abundance before the flaring event.

Bibliography

Aikawa, Y., Momose, M., Thi, W.-F., van Zadelhoff, G.-J., Qi, C., Blake, G. A., & van Dishoeck, E. F. 2003, PASJ, 55, 11

Aikawa, Y., Umebayashi, T., Nakano, T., & Miyama, S. M. 1999, ApJ, 519, 705

Ardila, D. R., Basri, G., Walter, F. M., Valenti, J. A., & Johns-Krull, C. M. 2002, ApJ, 567, 1013

Bergin, E. A., Aikawa, Y., Blake, G. A., & van Dishoeck, E. F. 2007, Protostars and Planets V, 751

Cleeves, L. I., Adams, F. C., & Bergin, E. A. 2013, ApJ, 772, 5

Cleeves, L. I., Bergin, E. A., Alexander, C. M. O. ., Du, F., Graninger, D., Öberg, K. I., & Harries, T. J. 2014, Science, 345, 1590

Cleeves, L. I., Bergin, E. A., Öberg, K. I., Andrews, S. M., Wilner, D. J., & Loomis, R. A. 2017, ArXiv e-prints

Cleeves, L. I., Öberg, K. I., Wilner, D. J., Huang, J., Loomis, R. A., Andrews, S. M., & Czekala, I. 2016, ApJ, 832, 110

Dutrey, A., Guilloteau, S., & Guelin, M. 1997, A&A, 317, L55

Dutrey, A., Henning, T., Guilloteau, S., Semenov, D., Piétu, V., Schreyer, K., Bacmann, A., Launhardt, R., Pety, J., & Gueth, F. 2007, A&A, 464, 615

Fogel, J. K. J., Bethell, T. J., Bergin, E. A., Calvet, N., & Semenov, D. 2011, ApJ, 726, 29

Garrod, R. T. 2013, ApJ, 765, 60

Getman, K. V., Feigelson, E. D., Broos, P. S., Micela, G., & Garmire, G. P. 2008, ApJ, 688, 418

Hasegawa, T. I., Herbst, E., & Leung, C. M. 1992, ApJS, 82, 167

Henning, T. & Semenov, D. 2013, Chemical Reviews, 113, 9016

Montmerle, T. & Casanova, S. 1996, in IAU Colloq. 153: Magnetodynamic Phenomena in the Solar Atmosphere - Prototypes of Stellar Magnetic Activity, ed. Y. Uchida, T. Kosugi, & H. S. Hudson, 247

Panić, O., Hogerheijde, M. R., Wilner, D., & Qi, C. 2009, A&A, 501, 269

Pinte, C., Padgett, D. L., Ménard, F., Stapelfeldt, K. R., Schneider, G., Olofsson, J., Panić, O., Augereau, J. C., Duchêne, G., Krist, J., Pontoppidan, K., Perrin, M. D., Grady, C. A., Kessler-Silacci, J., van Dishoeck, E. F., Lommen, D., Silverstone, M., Hines, D. C., Wolf, S., Blake, G. A., Henning, T., & Stecklum, B. 2008, A&A, 489, 633

Preibisch, T. & Feigelson, E. D. 2005, ApJS, 160, 390

Smith, I. W. M., Herbst, E., & Chang, Q. 2004, MNRAS, 350, 323

Stahler, S. W. & Palla, F. 2005, The Formation of Stars, 865

Wakelam, V., Cuppen, H. M., & Herbst, E. 2013, ArXiv e-prints

Williams, J. P. & Cieza, L. A. 2011, ARA&A, 49, 67

Wolk, S. J., Harnden, Jr., F. R., Flaccomio, E., Micela, G., Favata, F., Shang, H., & Feigelson, E. D. 2005, ApJS, 160, 423

CHAPTER 7

Appendix

TABLE 7.1 Model locations and parameters.

R AU	Z AU	ρ $\mathrm{gcm^{-3}}$	T_g K	T_{dust} K	UV Flux $\gamma \mathrm{s^{-1}cm^{-2}}$	X-ray Ionization $\mathrm{s^{-1}H_2^{-1}}$
1.0	0.0	1.07×10^{-9}	134.3	134.3	0.0	1.0×10^{-30}
1.0	0.1	2.49×10^{-10}	132.2	133.2	0.0	1.06×10^{-30}
1.0	0.2	7.03×10^{-12}	168.4	167.8	3.37×10^{10}	5.64×10^{-16}
1.0	0.3	7.29×10^{-15}	662	342.5	4.50×10^{14}	3.19×10^{-11}
1.0	0.4	1.98×10^{-18}	4200	341.1	5.82×10^{14}	1.63×10^{-10}
5.0	0.0	3.45×10^{-11}	60.9	61.0	0.0	1.0×10^{-30}
5.0	0.5	1.39×10^{-11}	60.8	61.0	0.0	3.53×10^{-22}
5.0	1.0	9.15×10^{-13}	75.3	75.8	3.50×10^{8}	1.55×10^{-17}
5.0	1.5	2.09×10^{-14}	145.9	141.5	4.06×10^{11}	1.88×10^{-14}
5.0	2.0	1.26×10^{-16}	820.5	164.9	2.54×10^{13}	5.854×10^{-12}
10.0	0.0	7.26×10^{-12}	43.9	44.0	0.0	7.66×10^{-27}
10.0	1.0	3.48×10^{-12}	44.4	44.3	0.0	2.91×10^{-22}
10.0	2.0	3.84×10^{-13}	52.9	52.9	2.41×10^{7}	2.73×10^{-18}
10.0	3.0	1.80×10^{-14}	90.2	88.5	3.58×10^{10}	1.23×10^{-15}
10.0	4.0	2.86×10^{-16}	259.1	121.1	5.76×10^{12}	7.40×10^{-13}
20.0	0.0	1.45×10^{-12}	26.1	26.1	0.0	2.41×10^{-25}
20.0	2.0	8.00×10^{-13}	27.3	28.0	0.0	1.60×10^{-21}
20.0	4.0	1.86×10^{-13}	32.3	34.0	9.25×10^{4}	2.82×10^{-19}
20.0	6.0	1.12×10^{-14}	53.7	56.0	4.58×10^{9}	7.91×10^{-17}
20.0	8.0	3.92×10^{-16}	117.4	90.2	7.90×10^{11}	3.95×10^{-14}

These are the parameters used for the 20 points used to represent the different radial distances and vertical heights in the model.

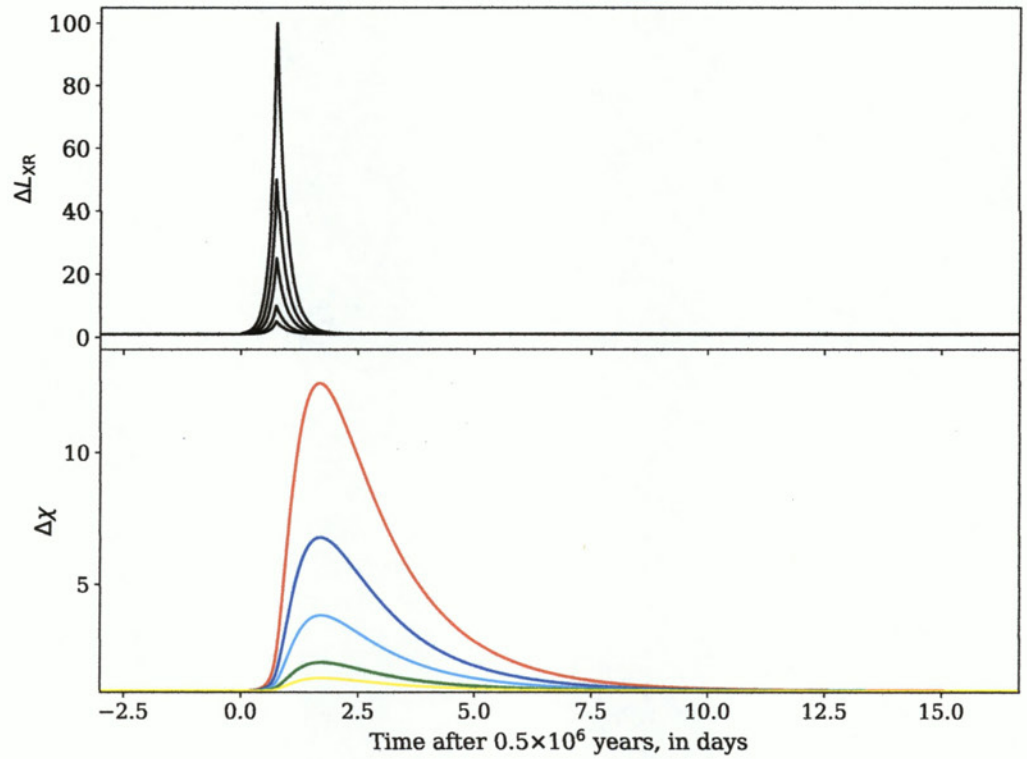

FIGURE 7.1 H_2O responses at R = 10AU Z/R = 0.4. Red indicates flare strength 100, blue indicates 50, cyan indicates 25, green indicates 10, and yellow indicates 5 times the background X-ray ionization rate. Note that the profile stays similar while the peak normalization changes with respect to the X-ray flare strength.

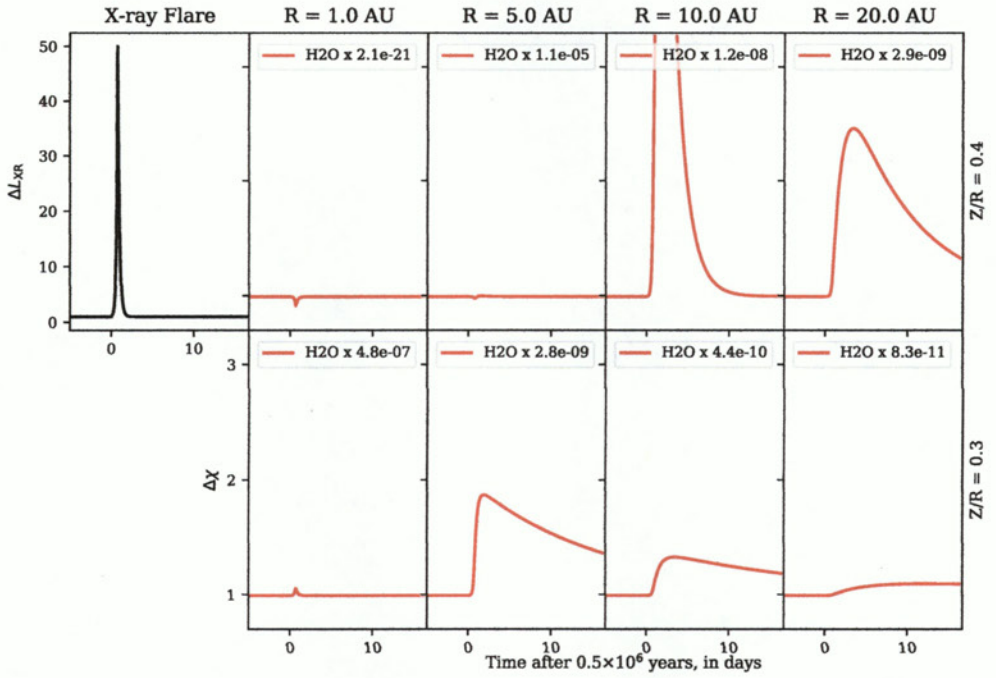

FIGURE 7.2 H_2O response grid with a flare strength of 50. See §3.2 Methods for other test parameters. Initial H_2O abundances appear at the top of each plot. See §4.6 for further discussion.

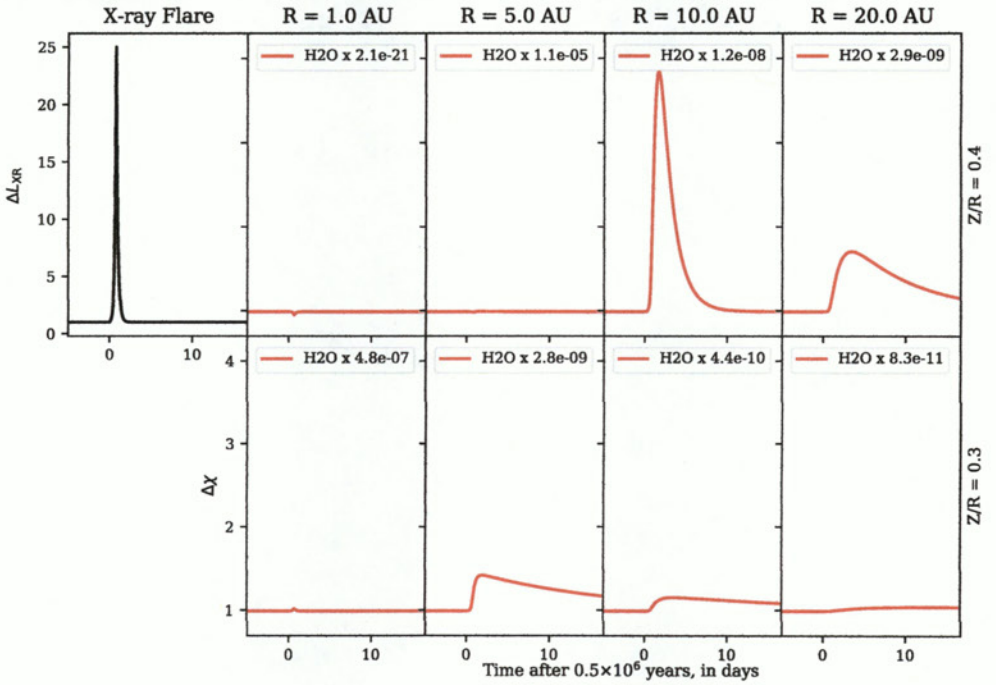

FIGURE 7.3 H_2O response grid with a flare strength of 25. See §3.2 Methods for other test parameters. Initial H_2O abundances appear at the top of each plot. See §4.6 for further discussion.

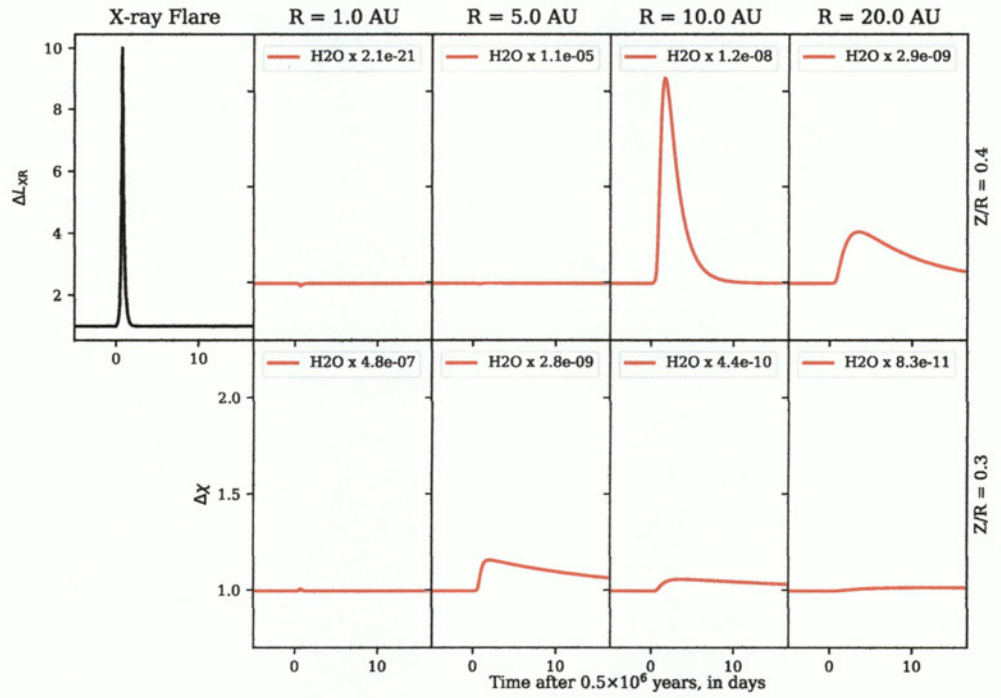

FIGURE 7.4 H_2O response grid with a flare strength of 10. See §3.2 Methods for other test parameters. Initial H_2O abundances appear at the top of each plot. See §4.6 for further discussion.

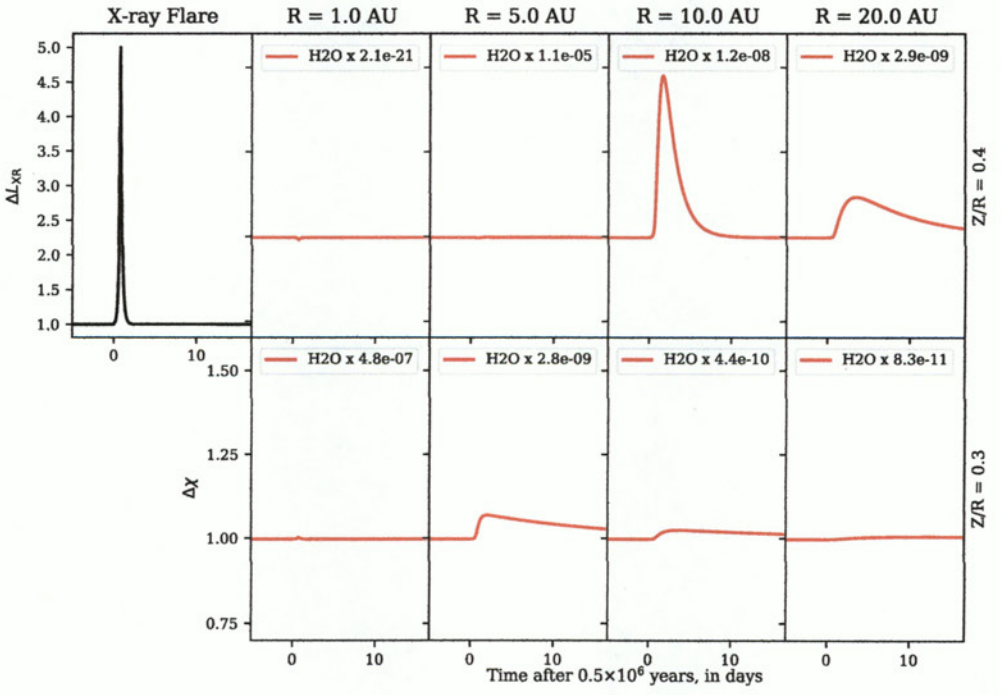

FIGURE 7.5 H_2O response grid with a flare strength of 5. See §3.2 Methods for other test parameters. Initial H_2O abundances appear at the top of each plot. See §4.6 for further discussion.